

A Decentralized Master-Slave Method for Three-Phase Cascaded H-Bridge System

Shi, Guangze; Han, Hua; Sun, Yao; Ou, Junlan; Lashab, Abderezak; Guerrero, Josep M.

Published in:

IEEE Journal of Emerging and Selected Topics in Industrial Electronics

DOI (link to publication from Publisher):

[10.1109/JESTIE.2023.3311172](https://doi.org/10.1109/JESTIE.2023.3311172)

Creative Commons License

CC BY-ND 4.0

Publication date:

2023

Document Version

Accepted author manuscript, peer reviewed version

[Link to publication from Aalborg University](#)

Citation for published version (APA):

Shi, G., Han, H., Sun, Y., Ou, J., Lashab, A., & Guerrero, J. M. (2023). A Decentralized Master-Slave Method for Three-Phase Cascaded H-Bridge System. *IEEE Journal of Emerging and Selected Topics in Industrial Electronics*, 4(4), 1110-1123. <https://doi.org/10.1109/JESTIE.2023.3311172>

General rights

Copyright and moral rights for the publications made accessible in the public portal are retained by the authors and/or other copyright owners and it is a condition of accessing publications that users recognise and abide by the legal requirements associated with these rights.

- Users may download and print one copy of any publication from the public portal for the purpose of private study or research.
- You may not further distribute the material or use it for any profit-making activity or commercial gain
- You may freely distribute the URL identifying the publication in the public portal -

Take down policy

If you believe that this document breaches copyright please contact us at vbn@aub.aau.dk providing details, and we will remove access to the work immediately and investigate your claim.

A Decentralized Master-slave Method for Three-Phase Cascaded H-bridge System

Guangze Shi, Hua Han, Yao Sun, Member, IEEE, Junlan Ou, Abderezak Lashab, Senior Member, IEEE and Josep M. Guerrero, Fellow, IEEE

Abstract— For the cascaded H-bridge system, the existing decentralized methods are mainly focused on single-phase systems. Designing a decentralized method for the three-phase cascaded H-bridge system is more challenging, particularly, for achieving phase-to-phase frequency synchronization and three-phase voltage balance without real-time communication among each distributed generation (DG). To achieve this, this paper proposes a decentralized master-slave method for three-phase cascaded H-bridge systems, where no communication is required for each local control unit of DGs. The overall control is divided into two parts. One part is for the master DG to realize phase synchronization among Phase-A, B, and C, which is designed by modifying the power factor angle through droop control. The other part is for slave DGs to achieve frequency synchronization of the modules in each phase, which adopts the power factor angle droop control. Small signal stability analysis based on fast and slow time scale separation is carried out for the proposed method. Last, the Control-hardware-in-loop (CHIL) tests and experimental results prove the effectiveness of the proposed method.

Index Terms—Decentralized control, Voltage balance, Cascaded H-bridge system.

I. INTRODUCTION

DGs have attracted more and more attention to alleviate the energy crisis due to their merits of scalability, cleanness, easy integration, and high flexibility. In recent years, the market of DGs has been growing rapidly and will project to account for more than half of global electricity production by 2035 [1]. The power electronic converter offers an effective way to connect multiple DGs, which can provide suitable power flow control and voltage regulation for each DG. Thus the power-electronic-enabled power system will obtain more operational flexibility and controllability comparable to conventional power systems,

which will become the future development trend [2], [3].

According to the interfacing power electronic converters topology, the DG system can be formed by parallel-connected or cascade-connected. The parallel-type form is evolved from the operation pattern of traditional power systems, which has been intensively investigated, including microgrids, distributed energy storage systems, and so on. Existing control methods for parallel-type DG systems emphasize droop control and virtual synchronous generator (VSG) control, which are inspired by the physical characteristics of synchronous generators. The droop control is often employed to achieve autonomous power sharing among DGs, based on the condition of the line impedance being mainly inductive [4], [5]. Alternatively, different from synchronous generators, the DGs system has either small or even no inertia and damping property to support grid frequency stability and even deteriorate it. The VSG control strategies are proposed in [6], [7] to overcome these problems, which make the system more stable and reliable under frequency fluctuation. However, most types of DGs have the characteristics of low-level voltage. So the parallel topology is difficult to operate in a high-voltage-level application.

The cascaded H-bridge topology offers an effective way for high voltage level application because it can easily boost voltage without bulky transformers and complex circuits. This topology can acquire simple voltage-scaling properties without expensive and bulky transformers. The cascaded H-bridge system (CHS) has been originally investigated for static synchronous compensators (STATCOMs) and motor drives [8] - [10]. Recently some authors developed this series topology into new energy applications for integrating low-voltage DGs (e.g. photovoltaics (PVs), energy storages) to medium/high voltage power networks [11] - [14]. For instance, the maximum allowed PV string voltage is 1kV in Europe, which makes the transformerless configuration using conventional converters unattainable. Furthermore, reviewing the existing literature, the CHSs usually operate with centralized control strategies [15] - [17] because it is easy to design the controller and achieve synchronized modulation. In this control structure, as shown in Table I, the central controller is responsible for all control signal generation and measurement collection. But when the number of cascaded modules increases, the increasing computational effort becomes a heavy burden for the central controller, if all control tasks are still centralized into a single central controller. Meanwhile, the switch commands are transmitted at every switching cycle, which should rely on high bandwidth communication.

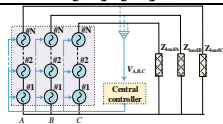
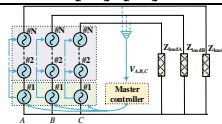
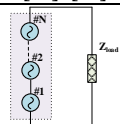
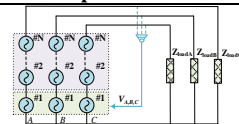
Manuscript received November 22, 2022; revised March 07, May 05 and July 21; accepted August 22. This work was supported in part by the National Science Fund for Distinguished Young Scholars under Grant 62125308, and the National Natural Science Foundation of China under Grant 52177205, 61933011, and 62192754. (Corresponding author: Hua Han.)

G. Shi is with the School of Artificial Intelligence and Advanced Computing, Hunan University of Technology and Business, Changsha, China, and also with the School of Automation, Central South University, Changsha, China. (e-mail: sgz001@foxmail.com)

H. Han, J. Ou and Y. Sun are with the School of Automation, Central South University and the Hunan Provincial Key Laboratory of Power Electronics Equipment and Gird, Changsha 410083, China (e-mail: hua_han@126.com, yaosun@csu.edu.cn, junlan@csu.edu.cn)

A. Lashab and J. M. Guerrero are with the Department of Energy Technology, Aalborg University, 9220 Aalborg (e-mail: ygu@et.aau.dk; joz@et.aau.dk).

TABLE I
COMPARISON WITH THE EXISTING METHODS

Features	[15] -[17]	[19] -[22]	[23] -[32]	Proposed method
Operation Configuration				
Control Configuration	Centralized	Distributed	Decentralized	Decentralized
Computation load	High	Middle	Low	Low
Synchronization Mechanism	Synchronization based on a central controller and high communication	Synchronization based on communication	Synchronization without communication	In-phase synchronization without communication Phase-to-phase synchronization based on PCC information
Communication Links	Central controller-all units Central controller-local&PCC sensors	Master-slave Master-PCC sensor	\	Master-PCC sensor
Communication Dependency	High	High	Low	Low
Resilient to communication failure	Low	Low	High	High
Voltage Balance	Ensured	Ensured	Not ensured	Ensured
Feasibility under Unbalance Load	Feasible	Feasible	Unfeasible	Feasible

To reduce the computational effort, the distributed control methods are preferred whose control structure is shown in Table I. In this structure, the fast time scale tasks, like PWM generators, voltage/current controllers [19], [20], and so on, are implemented by local controllers, while the central controller acts as the master to coordinate each local controller. For example, the authors in [21] propose a distributed control method to reduce the data transmission from the central controller to the local controllers. In [22], a distributed control considering communication delay and local control loop stability is proposed. However, when the DGs are geographically far apart, the communication burden for acquiring data and transmitting the control commands increases. Moreover, the possible failure of the communication network jeopardizes the stability and reliability of the CHS.

Inspired by droop control for paralleled-connecting systems, the researchers gradually focus on the decentralized control methods [23] -[25] that can generate their own voltage/frequency references directly within each local controller based on the local measurement. In decentralized structures, each DG can generate its own voltage/frequency references directly within each local controller based on the local measurement. Moreover, the system control can be localized, and each DG can be coordinated without communication. Thus, the communication dependency and computational load can be reduced simultaneously. In [23], an inverse power factor droop control scheme is first proposed to achieve frequency synchronization and proportional power sharing autonomously. The f - P/Q control [24] is designed with considering different types of loads which can expand the application scope. In [25], the unique-equilibrium-point decentralized method is proposed to overcome the multiple-

equilibrium-points problems. For grid-connection mode, [26] proposes a robust hybrid voltage/current synchronous control scheme that ensures communication-free grid connection of CHSs with a low communication burden. In [27], an ω -sin ϕ droop control is proposed, which can substantially weaken the effect of network pressure fluctuations on system stability. Moreover, a series of decentralized control methods are proposed for some specific applications, such as PVs [28], energy storage systems [29], STATCOM [30], series-connected H-bridge rectifiers [31], etc. In these methods, except for frequency synchronization, more control objectives are taken into consideration for each application's requirements, such as maximum power point (MPPT), battery state of charge (SOC) balancing, reactive power sharing, etc. Recently, to achieve unified control for both grid-connected and islanded modes, the power factor angle droop control is proposed in [32], which directly uses the power factor angles as feedback to achieve frequency synchronization. However, the aforementioned decentralized methods are only focusing on a single-phase CHS, which are not straightforwardly applied to three-phase CHS. The three-phase CHS has more complex and challenging control objectives, particularly achieving phase-to-phase frequency synchronization and three-phase voltage balance with only the local controller, and no real-time communication among each DG module.

To fill this research gap, this paper proposes a decentralized master-slave method for three-phase CHSs. In the proposed control scheme, the DG near the point of common coupling (PCC) is selected as the master of each phase, and the remaining $n-1$ DG units in each phase are regarded as slaves. The master DG should not only realize the frequency synchronization with the slave DGs but also ensure the phase-to-phase frequency

synchronization and three-phase voltage balance. The slaves in each phase can independently synchronize with the master unit based on the local controller. Thus, there is no communication link between the control units of the master and the slaves, which can reduce communication dependency and system costs. Compared with the traditional control approaches of three-phase CHS, as listed in Table I, the proposed control shows the following outstanding features: 1) The power control can be done locally in each module. Thus, the computation effort will be hugely reduced. 2) There is no communication between each local control unit, which will reduce the impact of the communication vulnerability risks over the control performance. 3) Compared with the decentralized methods of single-phase CHS, the proposed control method can achieve phase-to-phase and intra-phase frequency synchronizations simultaneously. Meanwhile, the three-phase voltage balance is guaranteed even under unbalanced load conditions. Simulation and experimental results have been conducted to validate the feasibility of the proposed control.

II. MOTIVATION

In this section, the motivation of this paper is discussed. The first is to introduce the three-phase CHS configuration. Fig. 1 presents the main circuit configuration of the three-phase CHS. Each phase (i.e. phases A, B, and C) is composed of n cascaded DGs with interfacing H-bridge converters with LC filter. The output voltages of the i -th converter in phases A, B, and C are denoted as $V_{Ai}e^{j\delta_{Ai}}$, $V_{Bi}e^{j\delta_{Bi}}$ and $V_{Ci}e^{j\delta_{Ci}}$, respectively. The coupling point voltages of phases A, B, and C are represented by $V_Ae^{j\delta_A}$, $V_Be^{j\delta_B}$ and $V_Ce^{j\delta_C}$, respectively. The relationship between the coupling point voltage and the voltages of all DG sources is expressed as follows:

$$V_x e^{j\delta_x} = \sum_{i=1}^n V_{xi} e^{j\delta_{xi}} \quad x = A, B \text{ or } C \quad (1)$$

It is easy to see that the three-phase CHS is comprised of three single-phase CHSs. There are interactions between in-phase and phase-to-phase units, which makes the coupling mechanism of the three-phase system more complex. The system must ensure the three-phase voltage balance based on frequency synchronization. This means that three-phase systems face more challenges.

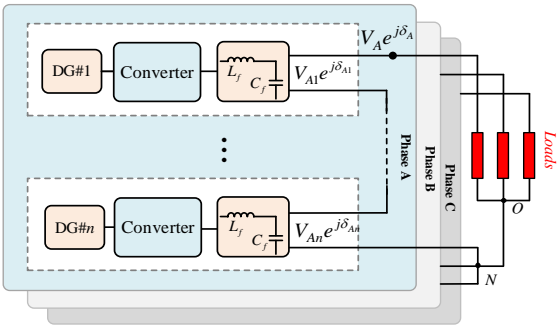


Fig. 1 Configuration of three-phase CHS.

1) More complex control objectives

Different from single-phase CHS, the most important objective is to guarantee the three-phase voltage balance. To achieve this, not only the frequency of DG unit in each single-

phase system but also the frequency between phases need to be synchronized at first.

$$\omega_{Ai} = \omega_{Aj} = \omega_{Bi} = \omega_{Bj} = \omega_{Ci} = \omega_{Cj} \quad (2)$$

What's more, the phases of each phase voltage need to be 120 degrees from each other and the voltage amplitude of each phase should be equal, which can be expressed as

$$\delta_A = \delta_B + \frac{2}{3}\pi = \delta_C - \frac{2}{3}\pi \quad (3)$$

$$V_A = V_B = V_C \quad (4)$$

Obviously, compared with the single-phase system, the control objectives for the three-phase one are more challenging.

2) Reasons for the challenges above

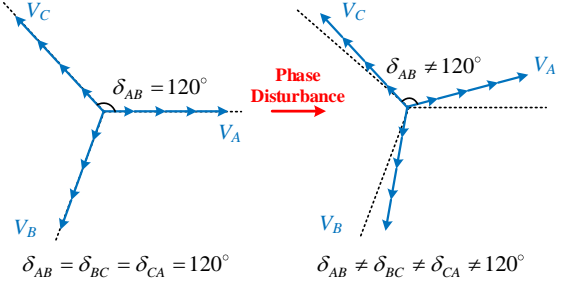


Fig. 2 Voltage angle unbalance diagrams.

There are two factors that will lead to voltage unbalance problems. The first one is voltage angle disturbance. As shown in Fig.2, due to the lack of phase balance constraint, the three-phase voltage phases of the system are prone to unbalance under external disturbances.

The second factor is unbalanced loads. In general, the load is not absolutely balanced. When the system load is unbalanced, the decentralized control relying only on local information will cause asynchronous frequency between phase subsystems. Taking the power factor angle droop control as an example, the frequency of each phase sub-system is a one-to-one correspondence with the load impedance angle of corresponding phase sub-systems.

$$\omega_{xi} = \omega_0 - m_x \varphi_{xi} = \omega_0 - m_x \theta_x \quad (5)$$

where θ_x represents the load impedance angle in the x -th phase.

From (5), it is obvious that unbalance loads will lead to frequency asynchronous among phase sub-systems.

$$\theta_A \neq \theta_B \neq \theta_C \Rightarrow \omega_{Ai} \neq \omega_{Bi} \neq \omega_{Ci} \quad (6)$$

III. PROPOSED CONTROL METHOD

To overcome the problems above, this paper proposes a decentralized master-slave control framework, as shown in Fig. 3. In this control framework, the three master units of each phase are controlled by a modified power factor control, which takes charge of coordinating the phase difference of each phase. The remaining units work autonomously and rely on local information. The detailed design and analysis of the proposed method are presented as follows.

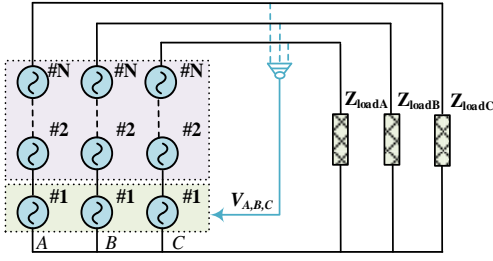


Fig.3 Proposed decentralized master-slave control framework

A. Design Principle

In this section, the design principle of the proposed control is discussed. To guarantee three-phase voltage balance, the core of the control design is to realize the controllability of frequency and voltage of each single-phase. Due to the restraints of the load and the power factor angle droop control, changing one of the DG power factor angles and voltage amplitude can adjust each phase system frequency and voltage. The voltage vector diagrams variation with changing one DG power factor angle φ_{xm} and voltage amplitude V_{xm} is described in Fig. 4.

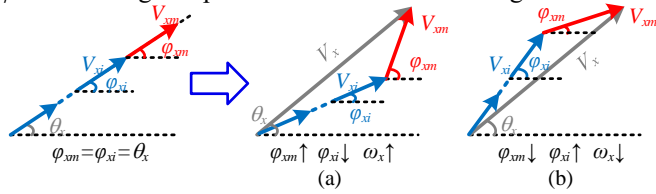


Fig. 4 Voltage vector diagrams variation with small fluctuation on DG power factor angle.

To analyze the phase frequency controllability, a small fluctuation is added to the DG power factor angle. It is assumed that the load impedance angle has no change before and after the small disturbance. From Fig. 4 (a), when the power factor angle of one DG increases, the remaining units will decrease their power factor angle. Thus, the frequency of the x -th phase system will increase. Similarity in Fig. 4 (b), decreasing the power factor angle of one DG will lead to a decrease in the x -th phase system frequency. Thus the phase frequency is adjustable.

Moreover, according to the cosine theorem, the voltage amplitude of each phase is derived.

$$V_x^2 = \left(\sum_{i=1, i \neq m}^n V_{xi} \right)^2 + V_{xm}^2 + 2 \left(\sum_{i=1, i \neq m}^n V_i \right) V_{xm} \cos(\varphi_{xm} - \varphi_{xi}) \quad (7)$$

From (7), it is obvious that the voltage amplitude of each phase can be regulated by modification of the power factor angle and voltage amplitude of one DG.

B. Proposed Method Design

In this paper, the overall control diagram is comprised of three-layer feedback loop control: power loop control, voltage loop control, and current loop control.

1) Power loop control

The power loop control is designed based on the power factor angle droop control, which takes the local power factor angle as feedback to modify the local frequency [32]. As for the slave DG unit, the power loop control is to achieve frequency synchronization among phase sub-system units, which is designed as follows

$$\omega_{xi} = \omega_0 - m_{xi} \varphi_{xi} \quad (8)$$

$$V_{xi} = V^* / n \quad (9)$$

$$V_{xi_ref} = \begin{cases} V_{xi} \sin(\int \omega_{xi} dt) & x=A \\ V_{xi} \sin(\int \omega_{xi} dt - 2\pi/3) & x=B \\ V_{xi} \sin(\int \omega_{xi} dt + 2\pi/3) & x=C \end{cases} \quad (10)$$

where ω_{xi} , φ_{xi} , V_{xi} and V_{xi_ref} are the angular frequency reference, power factor angle, voltage amplitude reference and voltage reference of the i -th DG in phase x , respectively. ω_0 represents the value of ω with no load. V^* is the nominal voltage amplitude value of the phase voltage. m_x is the adjustment droop coefficient for the DGs in phase x . It is noted that there is a frequency deviation in steady state. To make the system frequency vary in an acceptable range [49.5~50.5], the maximum value of the droop coefficient is derived as follows

$$m_{x_max} = 2\pi(f_{max} - f_{min}) / (\varphi_{max} - \varphi_{min}) = 2 \quad (11)$$

As for the master DG unit, the power loop control is designed by modifying the power factor droop control, which is expressed as follows

$$\begin{cases} \omega_{xL} = \omega_0 - m_x (\varphi_{xL} - \Delta\varphi_{xm}) \\ V_{xL} = u_{xm} V^* / n \end{cases} \quad (12)$$

$$V_{xL_ref} = \begin{cases} V_{xL} \sin(\int \omega_{xL} dt) & x=A \\ V_{xL} \sin(\int \omega_{xL} dt - 2\pi/3) & x=B \\ V_{xL} \sin(\int \omega_{xL} dt + 2\pi/3) & x=C \end{cases} \quad (13)$$

where ω_{xL} and V_{xL_ref} are the angular frequency reference and voltage reference of the master DG in x phase, respectively. δ_{xL0} represents the initial voltage angle. The $\Delta\varphi_{xm}$ and u_{xm} are the frequency modification and voltage reference modification, respectively.

The modification has two aspects. One is for the three-phase voltage angle balance, which is provided by the frequency modification $\Delta\varphi_{xm}$. Another one is for restoring the phase voltage amplitude in steady state, because the corresponding phase voltage amplitude will decrease when changing the master power factor angles. The frequency modification and voltage reference modification are designed as follows

$$\Delta\varphi_{xm} = \left(k_p + \frac{k_I}{s} \right) \sum_{j \in \Omega, j \neq x} (\delta'_j - \delta'_x) \quad (14)$$

$$u_{xm} = \sqrt{(2n-1) + (n-1)^2 \cos^2(\Delta\varphi_{xm})} - (n-1) \cos(\Delta\varphi_{xm}) \quad (15)$$

where $\Omega = \{A, B, C\}$. k_p and k_I are the frequency adjustment coefficient. $\delta'_A = \delta_A$, $\delta'_B = \delta_B + 2\pi/3$, $\delta'_C = \delta_C - 2\pi/3$.

2) Double voltage¤t loop control

The double voltage¤t loop control is used to track the voltage reference generated by power loop control. In this paper, the proportional-resonant (PR) control [33] is adopted for double voltage¤t loop control, because it is more suitable for tracking AC variable reference than PI control. The PR control voltage and current are designed as follows

$$G_v(s) = k_{pV} + \frac{2k_{rV} \cdot \omega_{cV} \cdot s}{s^2 + 2\omega_{cV} \cdot s + \omega_r^2} \quad (16)$$

$$G_i(s) = k_{pI} + \frac{2k_{rI} \cdot \omega_{cI} \cdot s}{s^2 + 2\omega_{cI} \cdot s + \omega_r^2} \quad (17)$$

where k_{pV} , k_{rV} , k_{pI} and k_{rI} are the proportional and resonant parameters of the double voltage¤t loop control, respectively. the ω_r , ω_{cV} and ω_{cI} are the resonant frequency and the cut-off frequency of the double voltage¤t loop control

Fig. 5 shows the simplified control block diagram of the closed-loop system. (a) slave controller, (b) master controller. As for the control block of the slave DG unit shown in Fig. 5(a), the local power factor angle is calculated as the feedback of the power control, which can modify the frequency reference value to regulate the output active and reactive powers. The following is the double voltage¤t loop control, which is to track the voltage reference generated by the power loop control. The feedback signals of the double voltage& current loop control are capacitance voltage and inductance current, respectively.

Fig. 5(b) represents the simplified control block diagram of the master controller. It is clear to see that the voltage and current loop control are the same as slave control. Different from the slave controller, the power loop control for the master controller is modified by phase voltage angle $\delta_{A,B,C}$, because the master control has responsibility for phase frequency synchronization and system voltage regulation. Specifically, a frequency modification is calculated by a consensus algorithm based on the phase voltage angle, which is to achieve phase-to-phase frequency synchronization. Also, a voltage modification is estimated by the vector triangular relation, which is to compensate for the voltage decrease caused by frequency modification.

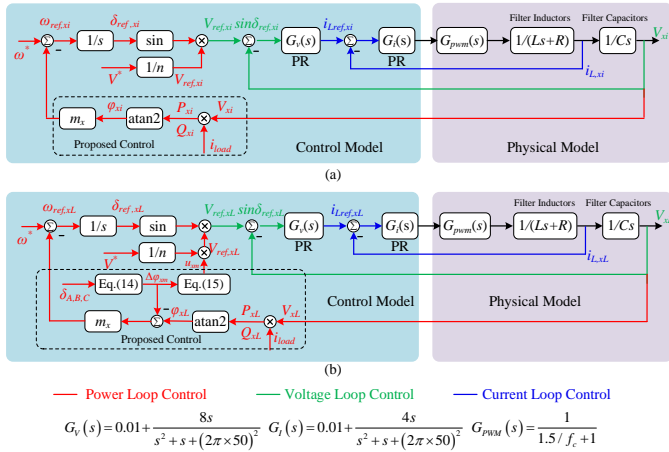


Fig. 5 Simplified control block diagram of the closed-loop system. (a) slave controller, (b) master controller

C. Steady-state analysis

In the steady state, based on the power factor angle droop controller [32], the frequency synchronization between the master and slave can be obtained.

$$\omega_{xL} = \omega_{xi} = \omega_x \quad x = A, B, C \quad (18)$$

In order to regulate the system voltage conveniently, it is necessary for the droop coefficients to be the same for the units in the same phase.

$$m_{AL} = m_{A2} = \dots = m_{An} \quad (19)$$

$$m_{BL} = m_{B2} = \dots = m_{Bn} \quad (20)$$

$$m_{CL} = m_{C2} = \dots = m_{Cn} \quad (21)$$

Moreover, it is easily obtained that the phase angle difference of the three-phase voltage is 120 degrees according to the Proportional-Integral (PI) controller, which is expressed as follows

$$\delta'_A = \delta'_B = \delta'_C \Rightarrow \delta_A = \delta_B + 2\pi/3 = \delta_C - 2\pi/3 \quad (22)$$

Also, the system should satisfy the power balance of supply and demand, so we can obtain

$$\begin{cases} V_x \cos \varphi_{Load} = \frac{u_{xm} V^*}{n} \cos \varphi_{xL} + \frac{(n-1)V^*}{n} \cos \varphi_{xi} \\ V_x \sin \varphi_{Load} = \frac{u_{xm} V^*}{n} \sin \varphi_{xL} + \frac{(n-1)V^*}{n} \sin \varphi_{xi} \end{cases} \quad (23)$$

Square the two formulas of (23) and then add them together,

$$V_x^2 = \left(\frac{V^*}{n} \right)^2 \left(u_{xm}^2 + (n-1)^2 + 2u_{xm}(n-1) \cos(\varphi_{xL} - \varphi_{xi}) \right) \quad (24)$$

All DGs in each phase share the same frequency. Based on the proposed control, the following formula (25) is obtained.

$$\varphi_{xL} - \varphi_{xi} = \Delta \varphi_{xm} \quad (25)$$

Substituting (15) and (25) into (24), it is derived that the voltage amplitude of each phase is the same.

$$V_x = V^* \quad (26)$$

From (22) and (26), the voltage balance of three-phase CHSs can be achieved in steady state.

The derivation of equation (22) is expressed as follows

$$\omega_A = \omega_B = \omega_C \quad (27)$$

Combining (18) and (27), the frequency synchronization of all units in the different phases is achieved

$$\omega_{AL} = \omega_{Ai} = \omega_A = \omega_{BL} = \omega_{Bi} = \omega_B = \omega_{CL} = \omega_{Ci} = \omega_C \quad (28)$$

IV. STABILITY ANALYSIS

According to the above analysis, the dynamic model of three-phase CHS can be summarized as follows

$$\begin{cases} \dot{\delta}_{xL} = \omega_{xL} - \omega_0 - m_x (\varphi_{xL} - \Delta \varphi_{xm}) \\ \dot{\delta}_{xi} = \omega_0 - m_x \varphi_{xi} \\ \Delta \dot{\varphi}_{xm} = k_P \sum_{j \in \Omega} (\delta'_j - \delta'_x) + k_I \sum_{j \in \Omega} (\delta'_j - \delta'_x) \end{cases} \quad (29)$$

A. Reduced Fast System Stability Analysis

Since the dynamic characteristics of the power factor controllers are much faster than the proposed modification, the studied system with the proposed control can be regarded as a two-time scale system. According to singular perturbation theory [34], when analyzing the reduced fast system, the slow variables can be considered as constant parameters. From (29), the small signal model of the reduced fast system can be expressed as

$$\begin{cases} \dot{\tilde{\delta}}_{xL} = -m_x \tilde{\varphi}_{xL} \\ \dot{\tilde{\delta}}_{xi} = -m_x \tilde{\varphi}_{xi} \\ \Delta \varphi_{xm} = \Delta \varphi_{xm}^c \\ u_{xm}^c = f(\Delta \varphi_{xm}^c) \end{cases} \quad (30)$$

where the superscript c represents that the variable is regarded as a constant value.

The power factor angle φ_{xi} is calculated based on local active power and reactive power information, which is derived as follows

$$\varphi_{xi} = \arctan \frac{Q_{xi}}{P_{xi}} = \arctan \frac{\sum_{j=1}^n V_{xi} \sin(\delta_{xi} - \delta_{xj} + \theta_x)}{\sum_{j=1}^n V_{xi} \cos(\delta_{xi} - \delta_{xj} + \theta_x)} \quad (31)$$

The small signal equation of (30) is derived as

$$\tilde{\varphi}_{xL} = \frac{B_x}{A_x} \sum_{j=1, j \neq L}^n (\tilde{\delta}_{xL} - \tilde{\delta}_{xj}) \quad (32)$$

$$\tilde{\varphi}_{xi} = \left(C_x (\tilde{\delta}_{xi} - \tilde{\delta}_{xL}) + B_x \sum_{j=1, j \neq L}^n (\tilde{\delta}_{xi} - \tilde{\delta}_{xj}) \right) / A_x \quad (33)$$

$$\begin{cases} A_x = u_{xm}^2 + (n-1)^2 + 2(n-1)u_{xm}^c \cos(\delta_{xL}^s - \delta_{xs}^s) \\ B_x = \left[u_{xm}^c \cos(\delta_{xs}^s - \delta_{xL}^s) + (n-1) \right] \\ C_x = \left[u_{xm}^2 + (n-1)u_{xm}^c \cos(\delta_{xs}^s - \delta_{xL}^s) \right] \end{cases} \quad (34)$$

where the superscript s represents steady state, \sim represents the small signal variable.

Substituting (31)~(34) to (30), and rewriting it in a matrix form gives

$$\dot{\tilde{\delta}} = -\mathbf{Y} \cdot \tilde{\delta} \quad (35)$$

$$\mathbf{Y} = \begin{bmatrix} \mathbf{M}_A \mathbf{Z}_A & 0 & 0 \\ 0 & \mathbf{M}_B \mathbf{Z}_B & 0 \\ 0 & 0 & \mathbf{M}_C \mathbf{Z}_C \end{bmatrix} \quad (36)$$

where \mathbf{E} below represents the identity matrix.

$$\mathbf{M}_x = m_x \mathbf{E} \quad (37)$$

$$\mathbf{Z}_x = \begin{bmatrix} \frac{(n-1)B_x}{A_x} & \frac{B_x}{A_x} & \dots & \frac{B_x}{A_x} \\ \frac{C_x}{A_x} & \frac{(n-2)B_x + C_x}{A_x} & \dots & \frac{B_x}{A_x} \\ \vdots & \vdots & \ddots & \vdots \\ \frac{C_x}{A_x} & \frac{B_x}{A_x} & \dots & \frac{(n-2)B_x + C_x}{A_x} \end{bmatrix} \quad (38)$$

According to the M-matrix theorem, the eigenvalues of \mathbf{Y} can be derived as the following

$$\lambda(\mathbf{Y}) = \{ \lambda(\mathbf{M}_A \mathbf{Z}_A), \lambda(\mathbf{M}_B \mathbf{Z}_B), \lambda(\mathbf{M}_C \mathbf{Z}_C) \} \quad (39)$$

First, the $\mathbf{M}_x \mathbf{Z}_x$ is the diagonally dominant matrix, the characteristic of which is derived as follows

$$|m_x \mathbf{Z}_{xii}| \geq \sum_{j=1, j \neq i}^n |m_x \mathbf{Z}_{xij}| \quad (40)$$

From (40), it can be observed that the gerschgorin region is on the right half plane. According to the gerschgorin circle theorem, the eigenvalues of $\mathbf{M}_x \mathbf{Z}_x$ fall within the gerschgorin regions. So it can be obtained that

$$\lambda(\mathbf{M}_x \mathbf{Z}_x) \geq 0 \quad (41)$$

From (41), the matrix \mathbf{Y} is a positive semi-definite with eigenvalues $0 = \lambda_1(\mathbf{Y}) < \lambda_2(\mathbf{Y}) \leq \dots \leq \lambda_{3n}(\mathbf{Y})$. The unique zero eigenvalue is corresponding to rotational symmetry, which does not affect the system stability [35]. Therefore, the stability of the reduced fast system is proved.

It is clear to see that $\lambda_2(\mathbf{Y})$ is the dominant pole that determines the rate of convergence.

$$\lambda_2(\mathbf{Y}) = m_x \max(\lambda_i(\mathbf{Z}_x) | \lambda_i(\mathbf{Z}_x) \neq 0) \quad (42)$$

According to (42), as m_x is larger than zero, the dominant

pole $\lambda_2(\mathbf{Y})$ will move away from the imaginary axis with increasing the m_x , which means that the response speed of the proposed control will be improved. However, the larger droop coefficient m_x will lead to an unallowable frequency deviation. Thus the value of m_x should take both response speed and frequency deviation into account.

Combined with the frequency deviation requirements (11), it is usually necessary to choose the droop coefficient as large as possible within the available range. However, the droop coefficient is not normally chosen to be the maximum value, because a margin is required depending on the practical requirements. Thus in this paper, the value of the droop coefficient is selected as follows

$$m_x = 0.9 \cdot m_{x_max} = 1.8 \quad (43)$$

B. Reduced Slow System Convergence Analysis

When analyzing a slower system, the dynamic of fast variables is considered as getting into steady state. Thus, the small signal model of the reduced slow system is derived as follows.

$$\begin{cases} \omega_{xL} = \omega_{xi} = \omega_x^s \\ \omega_x^s = \omega_0 - m_x \varphi_{xi} = \omega_0 - m_x (\theta_x - \Delta\varphi_{xi}) \\ \Delta\dot{\varphi}_{xm} = k_p \sum_{j \in \Omega} (\delta_j' - \delta_x') + k_I \sum_{j \in \Omega} (\delta_j' - \delta_x') \end{cases} \quad (44)$$

where $\Delta\varphi_{xi}$ represents slave power factor angle variation.

Combine formula (24) and rewrite formula (26),

$$n^2 = u_{xm}^2 + (n-1)^2 - 2u_{xm}(n-1)\cos(\pi - \Delta\varphi_{xm}) \quad (45)$$

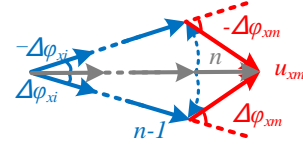


Fig. 6 Relationship between the master modification $\Delta\varphi_{xm}$ and slave power factor angle variation $\Delta\varphi_{xi}$.

According to the cosine theorem, the above triangle figure (Fig. 6) can be obtained, which reveals the relationship between the master modification $\Delta\varphi_{xm}$ and the slave power factor angle variation $\Delta\varphi_{xi}$. Based on the Law of Sines, the following can be obtained

$$\Delta\varphi_{xi} = \arcsin \left[\frac{u_{xm}}{n} \sin(\Delta\varphi_{xm}) \right] \quad (46)$$

Combining (23), yields,

$$\Delta\tilde{\varphi}_{xi} = D_x \Delta\tilde{\varphi}_{xm} \quad (47)$$

$$D_x = \left(\frac{u_{xm}^s (n-1) \sin^2 \Delta\varphi_{xm}^s}{u_{xm}^s + (n-1) \cos \Delta\varphi_{xm}^s} + u_{xm}^s \cos \Delta\varphi_{xm}^s \right) / \sqrt{n^2 - (u_{xm}^s \sin \Delta\varphi_{xm}^s)^2} \quad (48)$$

The $\Delta\varphi_{xm}$ should lie in $(-\pi/2, \pi/2)$, so the D_x is a constant greater than 0. Then the small signal model equation can be derived as follows

$$\begin{cases} \dot{\tilde{\delta}}_x = D_x m_x \Delta\tilde{\varphi}_{xm} \\ \Delta\dot{\tilde{\varphi}}_{xm} = k_p \sum_{j \in \Omega} (D_j m_j \Delta\tilde{\varphi}_{jm} - D_x m_x \Delta\tilde{\varphi}_{xm}) + k_I \sum_{j \in \Omega} (\tilde{\delta}_j - \tilde{\delta}_x) \end{cases} \quad (49)$$

Rewrite (49) in matrix form,

$$\begin{bmatrix} \dot{\tilde{\delta}}_x \\ \Delta\dot{\tilde{\varphi}}_{xm} \end{bmatrix} = \begin{bmatrix} 0 & \mathbf{DM} \\ -k_I \mathbf{L} & -k_p \mathbf{DML} \end{bmatrix} \begin{bmatrix} \tilde{\delta}_x \\ \Delta\tilde{\varphi}_{xm} \end{bmatrix} \quad (50)$$

where

$$\mathbf{D} = \text{diag} \{D_A, D_B, D_C\}_{3 \times 3} \quad (51)$$

$$\mathbf{M} = \text{diag} \{m_A, m_B, m_C\}_{3 \times 3} \quad (52)$$

$$\mathbf{L} = \begin{bmatrix} 2 & -1 & -1 \\ -1 & 2 & -1 \\ -1 & -1 & 2 \end{bmatrix} \quad (53)$$

Assuming that k_P and k_I are greater than zero, the Lyapunov energy function is defined as follows

$$V = \frac{1}{2} \Delta \tilde{\Phi}_m^T (\mathbf{D} \cdot \mathbf{M})^T \Delta \tilde{\Phi}_m + \frac{1}{2} k_I \tilde{\delta}^T \mathbf{L}^T \tilde{\delta} > 0 \quad (54)$$

The derivation of (48) is expressed as follows

$$\frac{dV}{dt} = -k_P \Delta \tilde{\Phi}_m^T (\mathbf{D} \cdot \mathbf{M})^T \mathbf{L} \cdot \mathbf{D} \cdot \mathbf{M} \cdot \Delta \tilde{\Phi}_m < 0 \quad (55)$$

According to the Lyapunov energy function method, if a given system can find a positive definite energy function V and satisfy $dV/dt < 0$, then the total energy of the system will gradually decrease and eventually reach a stable state. It is obvious that the reduced slow system is stable from formulas (54) and (55). The larger the control coefficient m and k_P will lead to the transient energy decreasing faster, the faster the transient energy decrease, which accelerates the system getting into the steady-state operation.

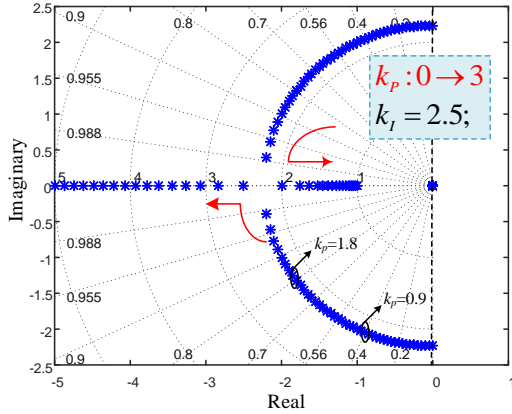


Fig. 7 Root locus change as k_P increases from 0 to 3.

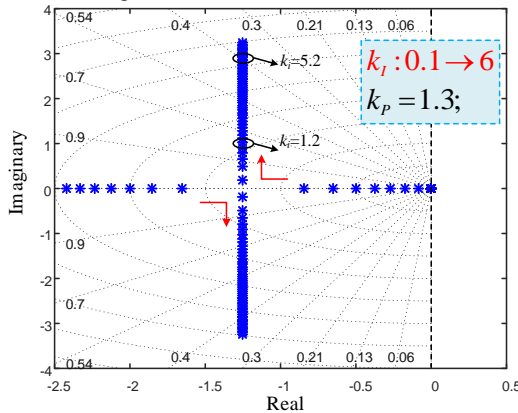


Fig. 8 Root locus change as k_I increases from 0.1 to 6.

To further discuss the selection range of k_P and k_I , the eigenvalue analysis of reduced slow system mode is presented. The influence of the control parameters on the

stability and dynamic performance of the system is clarified by the root locus analysis. From this, an approximate range of the control parameters selection can be obtained. In addition, it is noted that the parameters of eigenvalue analysis are the same as CHIL parameters.

Fig. 7 shows the root locus changing as the coefficient k_P varies from 0 to 3 while the k_I is set to be 2.5. As shown in Fig. 7, all eigenvalues lie on the left half plane, which can prove the stability of the system. When k_P increases, the conjugate poles move towards the real axis, which means that the oscillations will be decreased. To achieve better dynamic performance [36], the damping ratio is better to be constrained in [0.4, 0.8]. Thus, in this paper, the selection range of the coefficient k_P is [0.9, 1.8].

Fig. 8 shows the root locus changing as the coefficient k_I varies from 0.1 to 6 while the k_P is set to be 1.3. From Fig. 8, the stability of the system is proved by that all eigenvalues lie on the left half plane. When k_I increases, the dominant poles move away from the imaginary axis, which means that the oscillations will be increased. According to the aforementioned damping ratio range, the coefficient k_I is better to be constrained in [1.2, 5.2].

V. CHIL TESTS

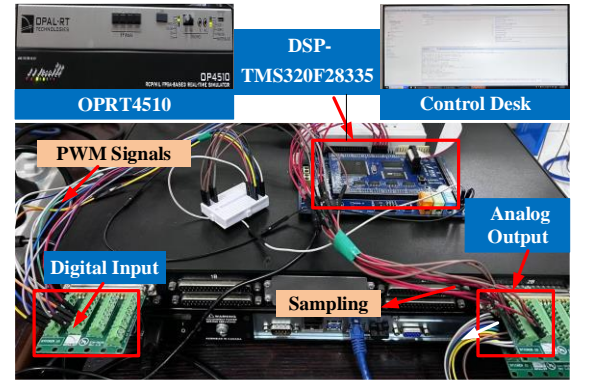


Fig. 9 Control-hardware-in-loop (CHIL) platform structure

TABLE II
CHIL PARAMETERS

Symbol	Item	Value
V^*	Voltage reference	311V
ω^*	Frequency reference	314rad
m	Droop control coefficient	1.8
f_c	PWM frequency	10kHz
n	DG number in each phase	3
L_f	Filter inductance	1.6mH
C_f	Filter capacitor	40uF
k_P	Frequency modification proportional coefficient	1.3
k_I	Frequency modification integral coefficient	2.5
k_{pV}	Proportional coefficient of voltage control	0.01
k_{rV}	Resonant coefficient of voltage control	8
ω_{cV}	Cut-off frequency of voltage control	0.5
k_{pI}	Proportional coefficient of current control	0.1
k_{rI}	Resonant coefficient of current control	4
ω_{cI}	Proportional coefficient of voltage control	0.5
ω_r	Resonant frequency of PR control	314rad

To verify the proposed control, a 3×3 cascaded H-bridge converters-based DGs system is designed in the CHIL platform,

as shown in Fig. 9. The main circuit including the three-phase cascaded H-bridge system, the LC filter, the line impedance, and the load are emulated in the OPAL-RT4510 simulator. The controller is implemented in the DSP-TMS320F28335 control board, and the sampling frequency is set to be 10kHz. The experimental data is recorded by the host machine of OPAL-RT4510. The topology of the system and the detailed control diagram are presented in Fig. 10. The main circuit and control parameters are listed in Table II.

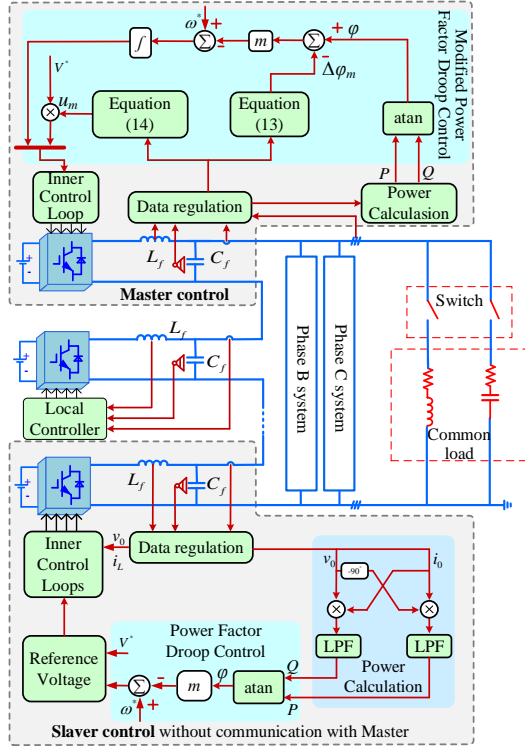


Fig. 10 Topology of the system and detailed control diagram.

A. Case I: Different initial phase angle

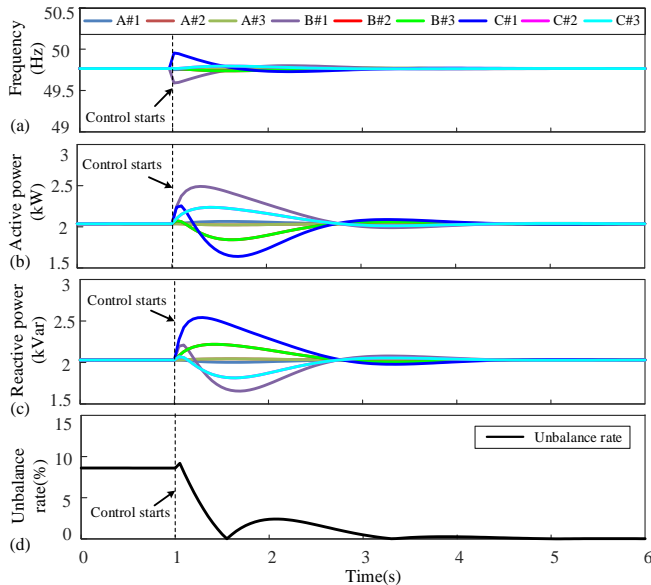


Fig. 11 Case I results: (a) frequency, (b) active power, (c) reactive power, (d) voltage unbalance rate.

The CHIL test results are shown in Fig. 11. To better illustrate the effectiveness, the different initial phase angles of converters are set at the beginning, 0 rad to the DG units in phase A, 0.15 rad to the DG units in phase B, -0.15 rad to the DG units in phase C. The RL load is set to $4+4j\Omega$. In the beginning, due to the different initial phase angles, the voltage unbalance reaches about 8.6%, which is out of the allowable range ($\leq 4\%$). After the proposed control starts, the voltage unbalance decreases evidently, and changes to zero eventually. Thus, the three-phase voltage balance is achieved in steady state. During the control working, the system can achieve voltage balance, frequency synchronization, and power sharing, which proves the feasibility of the proposed control.

B. Case II: Performance under unbalance load

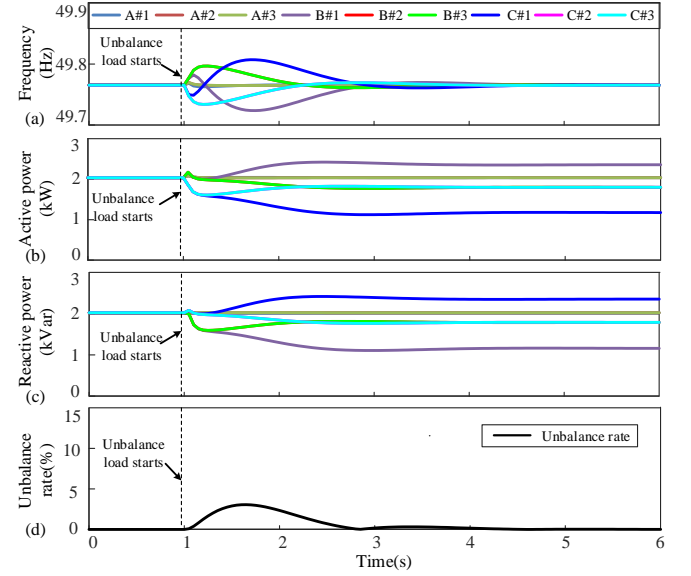


Fig. 12 Case II results: (a) frequency, (b) active power, (c) reactive power, (d) voltage unbalance rate

In this section, the feasibility of the proposed control under unbalance RL load is verified and the CHIL test results are presented in Fig. 12. In this case, the load will change from balance state to unbalance state. In detail, loads of phase A, B and C are changed from $4+4j\Omega$, $4+4j\Omega$ and $4+4j\Omega$ to $4+4j\Omega$, $5+4j\Omega$, and $4+5j\Omega$. After load change, the voltage unbalance is increased first and then decreased to zero, which means the voltage balance has already been achieved. Also, the active and reactive power dispatch is changing due to unbalance load, as shown in Fig. 12 (b) and (c). Although the power distribution has changed, the frequencies keep synchronized eventually after short fluctuation. Therefore, the proposed control works well under unbalance load.

C. Case III: load changing and load characteristic changing

Case III aims to illustrate the robustness of the proposed control under load changing and load characteristic changing. In the beginning, the system works under a balance three-phase load value ($8+2j\Omega$ for each phase). At $t=3s$, a large three-phase balance load about $6+2j\Omega$ is switched on. After load increases, as shown in Fig. 13 (a), the frequency is getting into another steady state point after a small disturbance. Moreover, the voltage unbalance rate and power sharing are still ensured. At

$t=11s$, the load for phase C is changed from RL load about $8+2j\Omega$ to RC load about $8-2j\Omega$. That is to say, the load changes from balanced state to unbalance state and there are existing different types of load in different phases. From Fig. 13 (a) and (d), despite large disturbances in frequency and voltage unbalance rate, the frequency synchronization is eventually achieved and the unbalanced rate reduces to 0 finally. In addition, the phase voltage amplitude returns to the normal rated value after a small disturbance. All in all, under different dynamic conditions, the CHIL results prove the robustness of the proposed control.

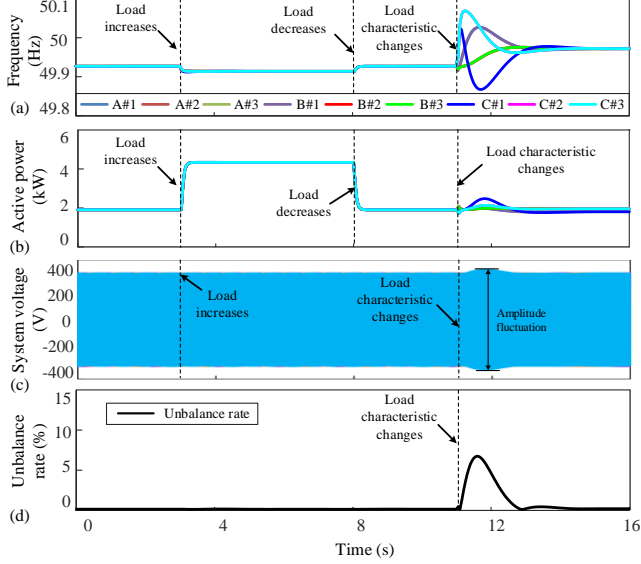


Fig.13 Case III results: (a) frequency, (b) active power, (c) system voltage, (d) voltage unbalance rate.

D. Case IV: performance under frequent-variation load

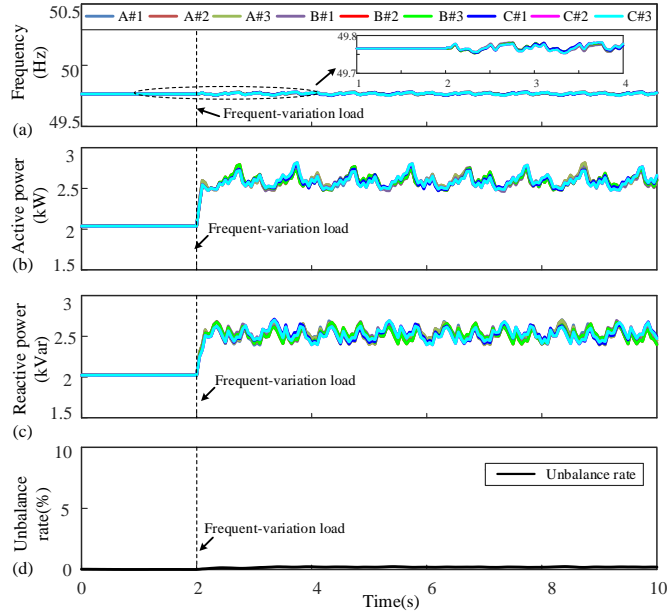


Fig. 14 Case IV results of frequent-variation balance load: (a) frequency, (b) active power, (c) reactive power, (d) voltage unbalance rate.

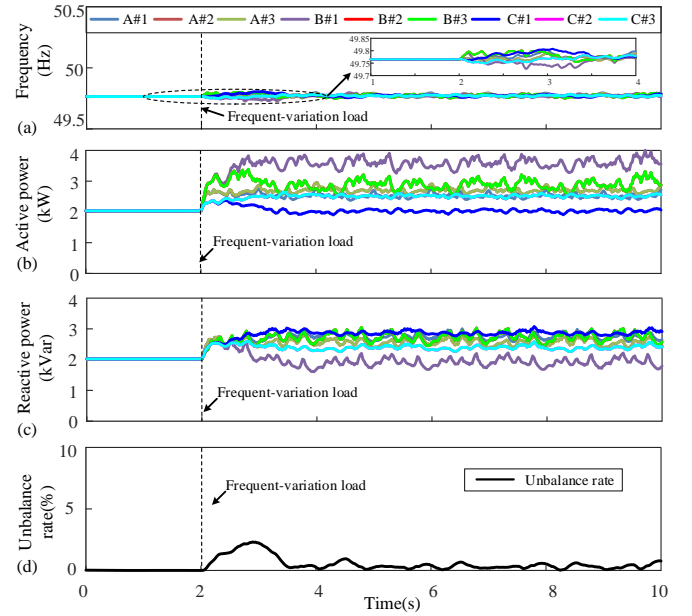


Fig. 15 Case IV results of frequent-variation unbalance load: (a) frequency, (b) active power, (c) reactive power, (d) voltage unbalance rate.

To further discuss the dynamic performance of the proposed method under frequent-variation load, two CHIL tests of the proposed control under frequent-variation balance load and unbalance load are carried out respectively. The frequent-variation load Z_{frl} is comprised of a resistor and an inductor connected in series, where $Z_{frl} = R_{frl} + jX_{frl}$. The resistance and inductance of the load are randomly selected between 10 and 20. Moreover, the load impedance values changed frequently, which is refreshed by a 20Hz pulse trigger signal.

Fig. 14 describes the CHIL result of the proposed control under a frequent-variation balance load. After inserting a frequent-variation balance load, the system has the ability to track rapidly changing loads, which proves the proposed control can achieve good dynamic performance. All units can still guarantee frequency synchronization and the active power of each unit can still maintain approximately equal distribution. Moreover, the unbalance rate can be reduced to 0.

The CHIL result of the proposed control under a frequent-variation unbalance load is shown in Fig. 15. As for frequent variation unbalance load, the resistances of the three-phase loads is still randomly selected between 10 and 20. The inductances of the load in phase A, B and C are randomly selected according to the following equation.

$$\begin{cases} X_{frlA} = \text{random}\{10,20\} \\ X_{frlB} = \text{random}\{0,10\} \\ X_{frlC} = \text{random}\{20,30\} \end{cases} \quad (56)$$

When the frequent-variation unbalance load is switched on, there are disturbances in frequency and voltage unbalance rate. It is clear to see from the partially enlarged view of Fig.15 (a) that the frequency can still converge after fluctuating. Moreover, although the unbalance rate cannot be reduced to 0 due to the frequent-variation unbalance load, it can still be guaranteed to be within the safe range.

All in all, despite working under frequent-variation loads, the proposed control method is still effective.

E. Case V: Comparison between the three-phase CHS with and without neutral-point connection

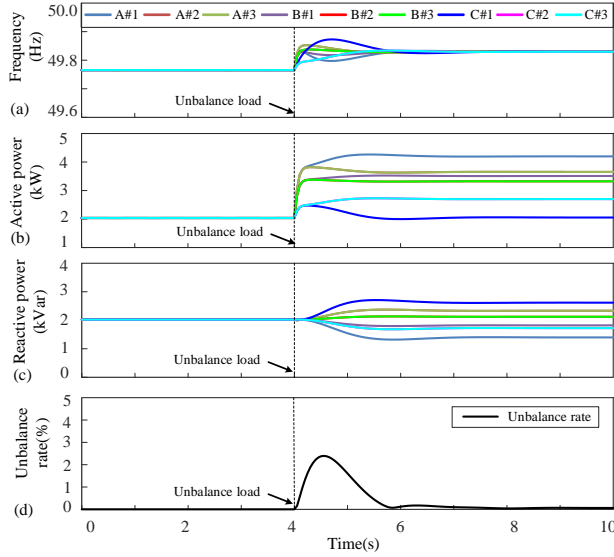


Fig. 16 Case V results of three-phase CHS with neutral-point connection: (a) frequency, (b) active power, (c) reactive power, (d) voltage unbalance rate.

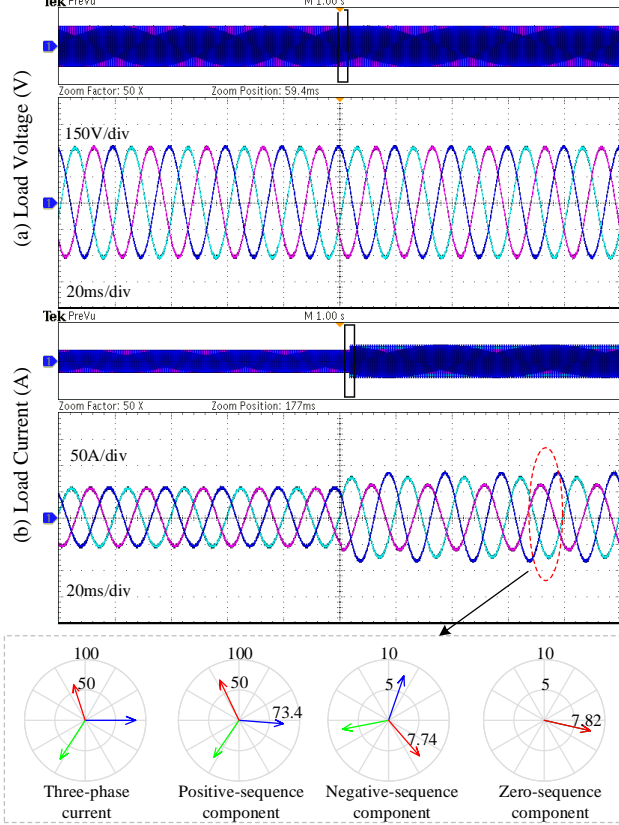


Fig. 17 Case V waveforms of three-phase CHS with neutral-point connection.

In this case, a comparison CHIL test has been added for three-phase CHS with and without neutral-point connection. To discuss their difference, the case of adding an unbalance load is selected. In the beginning, the system works under a balance three-phase load value ($4+4j\Omega$ for each phase). At $t=4$ s, a three-phase unbalance load (9Ω , 12Ω and 36Ω for phase A, B, and C, respectively) is added. Fig. 16 and 17 are the CHIL test

results and waveforms of three-phase with neutral-point connection, respectively. Fig. 18 and 19 present the CHIL test results and waveforms of three-phase without neutral-point connection, respectively.

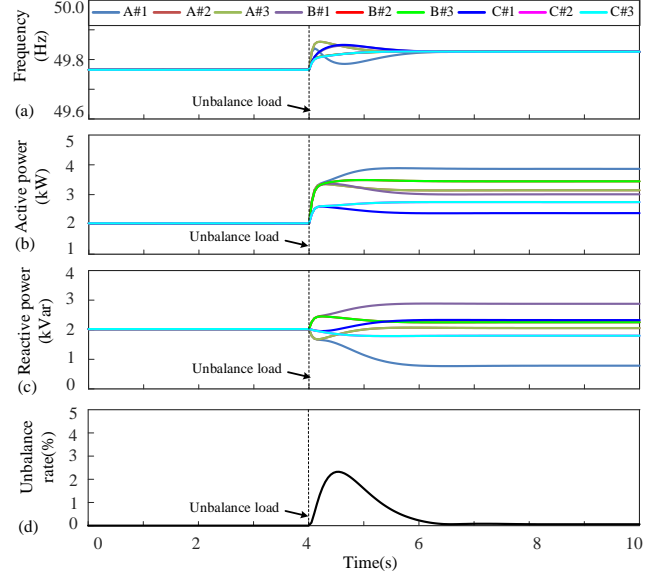


Fig. 18 Case V results of three-phase CHS without neutral-point connection: (a) frequency, (b) active power, (c) reactive power, (d) voltage unbalance rate.

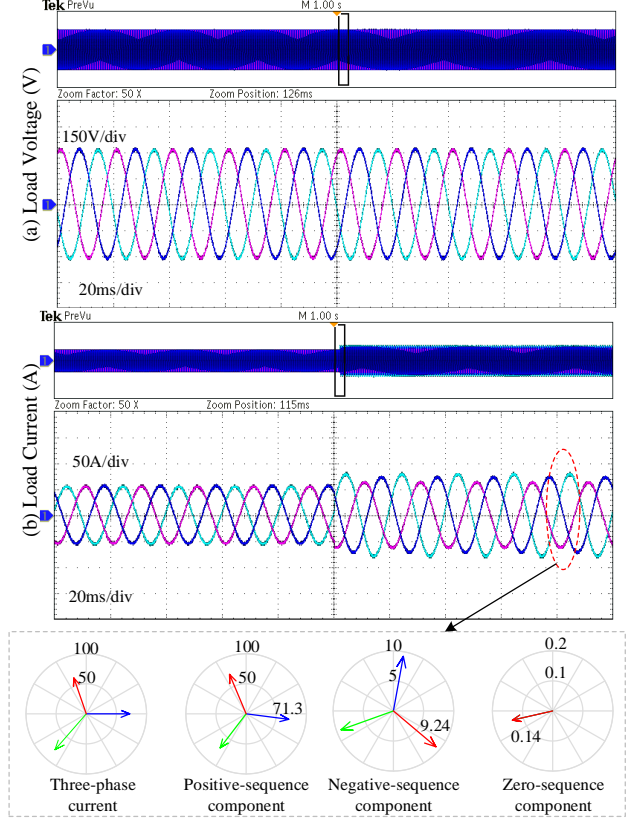


Fig. 19 Case V waveforms of three-phase CHS without neutral-point connection.

When working under balance load before 4s, the frequency synchronization, power sharing, and three-phase voltage can be achieved in both two comparison cases. Moreover, in steady state, the two comparison cases can share the same value of the

steady-state frequency, active power and reactive power. As for balance load, there is no difference for the three-phase CHS with and without neutral-point connection. Thus, the feasibility under balance load without neutral-point connection is verified. After $t=4s$, the system adds an unbalance load. The variation of frequency, active and reactive power are different between the three-phase CHS with and without neutral-point connection. But in both comparison cases, as shown in Fig. 16 (a) (b) and Fig. 18 (a) (b), the frequency synchronization and three-phase voltage balance can be achieved after fluctuation. Moreover, it can be seen from the waveform figure (Fig. 17 and Fig. 19) that the voltage can still maintain balance and the current can be quickly tracked after the unbalanced load is cut in. Due to the different structure, the steady-state currents are also different. To analyze their difference, the three-phase unbalance currents are decomposed into positive-sequence, negative-sequence, and zero-sequence currents based on symmetrical component method. As for the system with neutral-point connection, the system has negative-sequence and zero-sequence currents. As for the system without neutral-point connection, the system only has negative-sequence current and no zero-sequence current. The main reason for this difference is that zero-sequence current generally only exists in systems with neutral-point connection or neutral-point grounding. All in all, when under unbalance load, the feasibility of the system without neutral-point connection is proved. Although the proposed control method has some differences in steady-state performance between the two comparison systems, the frequency synchronization, three-phase voltage balance, and stable operation can be still achieved.

VI. EXPERIMENTAL RESULTS

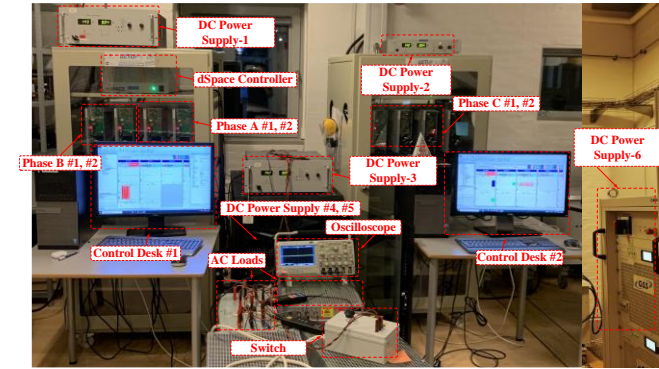


Fig. 20. The hardware experimental setups of the cascaded three-phase system.

TABLE III

EXPERIMENTAL PARAMETERS

Symbol	Item	Value
V^*	Voltage reference	200V
ω^*	Frequency reference	314rad
m	Droop control coefficient	1.8
f_c	PWM frequency	10kHz
T_s	Sampling time	1e-4s
n	DG number in each phase	2
L_f	Filter inductance	1.8mH
C_f	Filter capacitor	25uF
k_p	Frequency modification proportional coefficient	1.3
k_i	Frequency modification integral coefficient	2.5

The hardware experimental tests are conducted at the *Intelligent Microgrid Lab* at Aalborg University [37]. The experimental setup is shown in Fig. 20, which consists of six DC power supplies, six inverters, two dSPACE controllers, and AC loads. In these experiment tests, each phase system is comprised of two cascaded DGs. The dSPACE 1006 platform is programmed, where the program is compiled under Matlab/Simulink. The experimental parameters are listed in Table III.

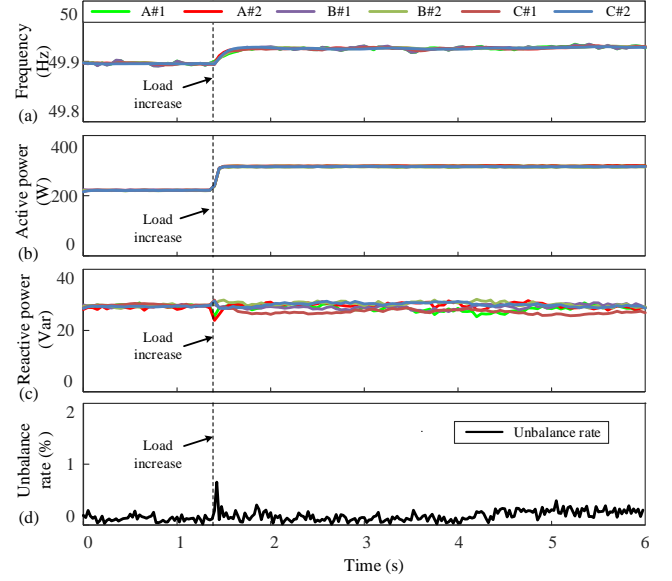


Fig. 21. Experimental results of case I. (a) frequency, (b) active power, (c) reactive power, (d) voltage unbalance rate.

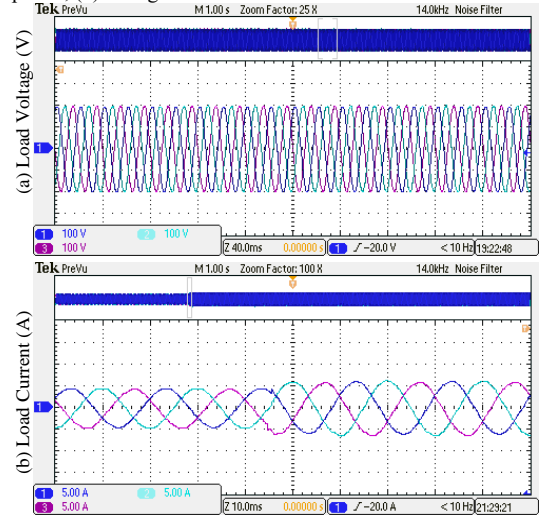


Fig. 22. Experimental waveforms of the proposed control under load changes.

A. Case I: Performance under load changes

The performance and waveform of the proposed control under load change are demonstrated in Fig. 21 and Fig. 22. As shown in Fig. 21 (a), after the load increases, the frequencies of all units increase a little after fluctuation. This is because the increasing load characteristic is resistive, which will decrease the power factor angle. Except that there is a small step response during the load change, the voltage unbalance rate remains almost constant at zero. From Fig. 22, the voltage amplitudes of each phase remain at 200V in steady state, where the dynamic

response of the current is fast. Moreover, frequency synchronization, voltage balance, and power sharing are guaranteed. In short, the above experimental results prove the effectiveness of the proposed control strategy in case of load changes.

B. Case II: Comparison between the proposed control and the traditional power factor angle droop control

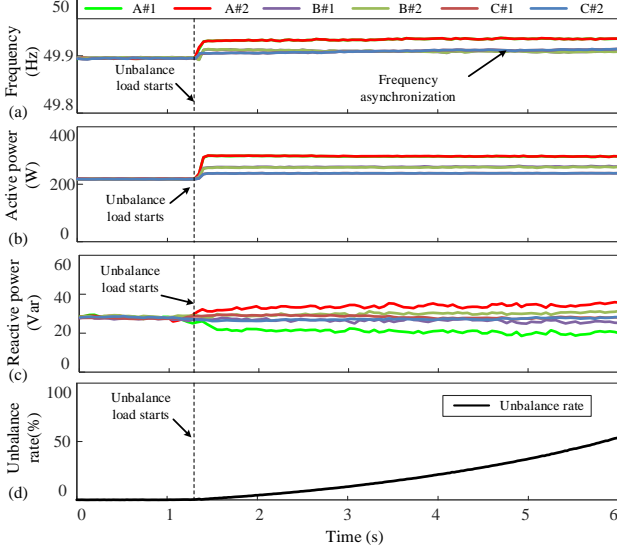


Fig. 23. Experimental results of traditional decentralized control. (a) frequency, (b) active power, (c) reactive power, (d) voltage unbalance rate.

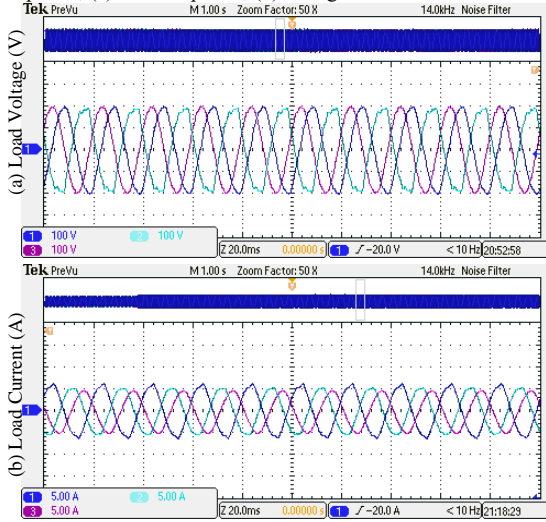


Fig. 24. Experimental waveforms of the traditional decentralized control under unbalance load.

In case of working under an unbalance load, an experimental comparison test between the proposed control and the traditional power factor angle droop control is conducted. As shown in Fig. 23, when the unbalanced load is switched on, the frequency of each phase cannot achieve synchronization and the voltage unbalance rate increases rapidly. From Fig. 24, it is clear to see that the three-phase voltages cannot be kept balanced. Moreover, it suffers from voltage and current distortions. In contrast, as observed from Fig. 25, when introducing the unbalance load, the phase frequency synchronization can be achieved and the voltage unbalance rate

returns to 0 after a small fluctuation. Not only that, Fig. 26 represents that the three-phase voltage can be kept balanced and the voltage amplitude can remain at the normal value, which means that the system has better voltage quality.

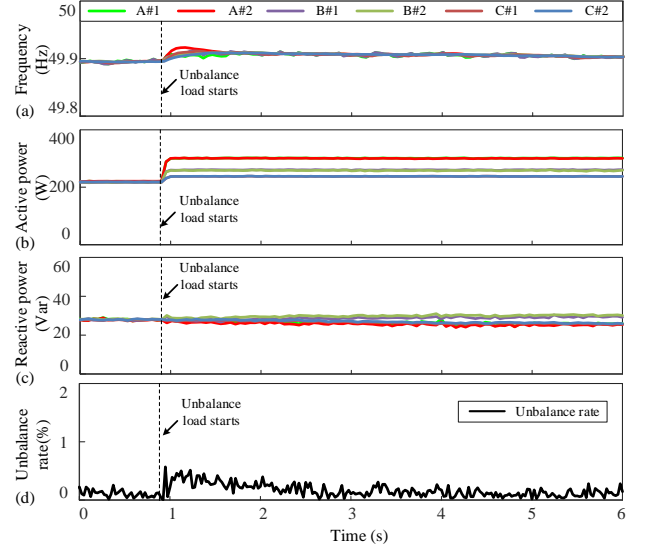


Fig. 25. Experimental results of the proposed control. (a) frequency, (b) active power, (c) reactive power, (d) voltage unbalance rate..

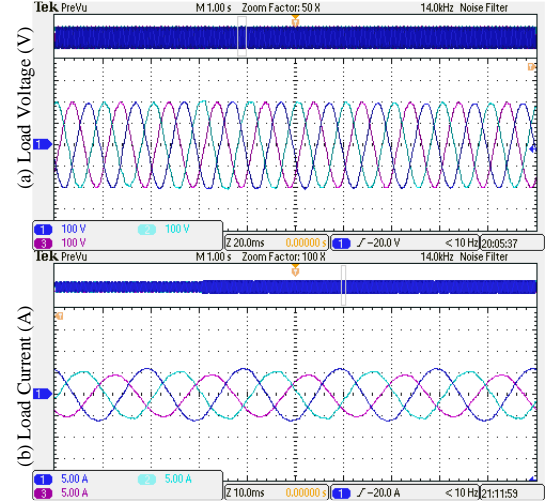


Fig. 26. Experimental waveforms of the proposed control under unbalance load.

VII. CONCLUSIONS

In this paper, a decentralized master-slave control method is proposed for the three-phase cascaded H-bridge system. In each phase sub-system, one DG is assigned to be the master, while the rest are slaves. Different from the existing master-slave control framework, the proposed control can ensure communication-less operation among all DGs. In detail, as for master DG, a modified power factor droop control is designed to guarantee the system voltage balance and keep the normal operation under an unbalanced load. Also, the slave DGs are worked under individual power factor droop control with local measurements, which ensures frequency synchronization in each phase. Due to no communication between the local control units of the master and slave, the risk of communication failure and the cost are decreased, which also increases system

reliability to a certain extent. Moreover, the stability has been proved based on the singular perturbations theory. Finally, the CHIL tests and experimental results have validated the feasibility of the proposed method.

REFERENCES

- [1] McKinsey & Company, "Global Energy Perspective 2019"
- [2] N. Hatziaargyriou, H. Asano, R. Iravani, and C. Marnay, "Microgrids," *IEEE Power and Energy Magazine*, vol. 5, no. 4, pp. 78-94, 2007.
- [3] R. H. Lasseter, "MicroGrids," in 2002 IEEE Power Engineering Society Winter Meeting. Conference Proceedings (Cat. No.02CH37309), 2002, vol. 1, pp. 305-308 vol.1.
- [4] N. Pogaku, M. Prodanovic, and T. C. Green, "Modeling, Analysis and Testing of Autonomous Operation of an Inverter-Based Microgrid," *IEEE Trans. on Power Electronics*, vol. 22, no. 2, pp. 613-625, 2007.
- [5] J. Rocabert, A. Luna, F. Blaabjerg, and P. Rodríguez, "Control of Power Converters in AC Microgrids," *IEEE Transactions on Power Electronics*, vol. 27, no. 11, pp. 4734-4749, 2012.
- [6] Zhong, Q.C., Phi-Long, N., Ma, Z.Y., et al.: 'Self-synchronized synchronverters: inverters without a dedicated synchronization unit', *IEEE Trans. Power Electron.*, 2014, 29, (2), pp. 617-630
- [7] Fang, J., Tang, Y., Li, H., et al.: 'A battery/ultracapacitor hybrid energy storage system for implementing the power management of virtual synchronous generators', *IEEE Trans. Power Electron.*, 2018, 33, (4), pp.2820-2824
- [8] P. W. Hammond, "A new approach to enhance power quality for medium voltage ac drives," *IEEE Trans. Ind. Appl.*, vol. 33, no. 1, pp. 202-208, Jan./Feb. 1997.
- [9] R. H. Osman, "A medium-voltage drive utilizing series-cell multilevel topology for outstanding power quality," in *Conf. Rec. IEEE IAS Annu. Meet.*, 1999, vol. 4, pp. 2662-2669.
- [10] H. Akagi, S. Inoue, and T. Yoshii, "Control and performance of a transformerless cascade PWM STATCOM with star configuration," *IEEE Trans. Ind. Appl.*, vol. 43, no. 4, pp. 1041-1049, Jul./Aug.2007.
- [11] Yang, X., Song, Y., Wang, G., et al.: 'A comprehensive review on the development of sustainable energy strategy and implementation in China', *IEEE Trans. Sustain. Energy*, 2010, 1, (2), pp. 57-65
- [12] Liang, X.: 'Emerging power quality challenges due to integration of renewable energy sources', *IEEE Trans. Ind. Appl.*, 2017, 53, (2), pp. 855-866
- [13] N. Moeini, M. Bahrani-Fard, M. Shahabadani, S. M. Azimi and H. Iman-Eini, "Passivity-Based Control of Single-Phase Cascaded H-Bridge Grid-Connected Photovoltaic Inverter," *IEEE Transactions on Industrial Electronics*, vol. 70, no. 2, pp. 1512-1520, Feb. 2023.
- [14] Yao, L., Yang, B., Cui, H., et al.: 'Challenges and progresses of energy storage technology and its application in power systems', *J. Mod. Power Syst.Clean Energy*, 2016, 4, (4), pp. 519-528
- [15] Maharjan, L., Inoue, S., Akagi, H., et al.: 'State-of-charge (SOC)-balancing control of a battery energy storage system based on a cascade PWM converter', *IEEE Trans. Power Electron.*, 2009, 24, (6), pp. 1628-1636
- [16] Zhao, H., Yang, Q., Zeng, H.: 'Multi-loop virtual synchronous generator control of inverter-based DGs under microgrid dynamics', *IET Gener. Transm. Distrib.*, 2017, 11, (3), pp. 795-803
- [17] X. Shi, C. Zhang, R. Li and X. Cai, "Control Scheme for Second Harmonic Current Elimination in Single-Star Configuration Based Cascade Multilevel Energy Storage System," in *IEEE Journal of Emerging and Selected Topics in Industrial Electronics*, vol. 3, no. 4, pp. 1210-1216, Oct. 2022.
- [18] Y. Xie et al., "A Simplified Algorithm of Finite Set Model Predictive Control for Three-Phase CHB-based BESSs," *IEEE Journal of Emerging and Selected Topics in Power Electronics*, early access, 2023.
- [19] P. C. Loh, D. G. Holmes, and T. A. Lipo, "Implementation and control of distributed PWM cascaded multilevel inverters with minimal harmonic distortion and common-mode voltage," *IEEE Trans. Power Electron.*, vol. 20, no. 1, pp. 90-99, Jan. 2005
- [20] S. Yang, P. Wang and Y. Tang, "Feedback Linearization-Based Current Control Strategy for Modular Multilevel Converters," *IEEE Transactions on Power Electronics*, vol. 33, no. 1, pp. 161-174, Jan. 2018
- [21] S. Huang, R. Teodorescu, and L. Mathe, "Analysis of communication based distributed control of MMC for HVDC," in *Proc. 2013 15th Eur. Conf. Power Electron. Appl.*, 2013, pp. 1-10.
- [22] L. Mathe, P. D. Burlacu, and R. Teodorescu, "Control of a modular multilevel converter with reduced internal data exchange," *IEEE Trans. Ind. Inform.*, vol. 13, no. 1, pp. 248-257, Feb. 2017.
- [23] J. He, Y. Li, B. Liang, and C. Wang, "Inverse Power Factor Droop Control for Decentralized Power Sharing in Series-Connected Microconverters-Based Islanding Microgrids," *IEEE Transactions on Industrial Electronics*, vol. 64, no. 9, pp. 7444-7454, 2017.
- [24] Y. Sun et al., "An f-P/Q Droop Control in Cascaded-Type Microgrid," *IEEE Trans. on Power Systems*, vol. 33, no. 1, pp. 1136-1138, 2018
- [25] Lang Li, Yao Sun, Zhangjie Liu, Xiaochao Hou, Guangze Shi, Mei Su."A Decentralized Control with Unique Equilibrium Point for Cascaded-type Microgrid," *IEEE Transactions on Sustainable Energy*, vol. 10, no. 1, pp. 324-326, Jan. 2019.
- [26] X. Hou, K. Sun, X. Zhang, Y. Sun and J. Lu, "A Hybrid Voltage/Current Control Scheme With Low-Communication Burden for Grid-Connected Series-Type Inverters in Decentralized Manner," *IEEE Transactions on Power Electronics*, vol. 37, no. 1, pp. 920-931, Jan. 2022, doi: 10.1109/TPEL.2021.3093080.
- [27] X. Hou, K. Sun, X. Zhang, Y. Sun and J. Lu, "An Improved Decentralized Control of Cascaded Inverters with Robust Stability against Grid-Voltage Variation," *IEEE Transactions on Energy Conversion*, doi: 10.1109/TEC.2021.3109797.
- [28] Xiaochao Hou, Yao Sun*, Hua Han, Zhangjie Liu, Wenbin Yuan, Mei Su."A Fully Decentralized Control of Grid-Connected Cascaded Inverters," *IEEE Transactions on Sustainable Energy* , vol.10, no.1, pp. 315-317, 2019.
- [29] Guangze Shi, Hua Han, Yao Sun, Zhangjie Liu, Minghui Zheng and Xiaochao Hou "A Decentralized SOC Balancing Method for Cascaded-type Energy Storage System," *IEEE Transactions on Industrial Electronics*, early access, 2020
- [30] Xiaochao Hou, Yao Sun, Hua Han, Zhangjie Liu, Mei Su, Benfei Wang and Xin Zhang."A General Decentralized Control Scheme for Medium/High Voltage Cascaded STATCOM," *IEEE Transactions on Power Systems*, vol.33, no.6, pp7296-7300, Nov. 2018.
- [31] Xiaochao Hou, Yao Sun, Xin Zhang, Guanguan Zhang, Jinghang Lu, Frede Blaabjerg "A Self-Synchronized Decentralized Control for Series-Connected H-bridge Rectifiers," *IEEE Transactions on Power Electronics*, vol. 34, no. 8, pp. 7136-7142, Aug. 2019.
- [32] Y. Sun, L. Li, G. Shi, X. Hou and M. Su, "Power Factor Angle Droop Control—A General Decentralized Control of Cascaded Inverters," *IEEE Transactions on Power Delivery*, vol. 36, no. 1, pp. 465-468, Feb. 2021.
- [33] Hua Y , Cordoba-Arenas A , Warner N , et al. "A multi time-scale state-of-charge and state-of-health estimation framework using nonlinear predictive filter for lithium-ion battery pack with passive balance control". *Journal of Power Sources*, vol. 280, pp:293-312, Jan. 2015
- [34] A. Narang-Siddarth and J. Valasek, *Nonlinear Time Scale System in Standard and Nonstandard Forms: Analysis and Control*. Society for Industrial and Applied Mathematics, 2014
- [35] J. W. Simpson-Porco, F. Dorfler, and F. Bullo, "Synchronization and power sharing for droop-controlled inverters in islanded microgrids," *Automatica*, vol. 49, no. 9, pp. 2603-2611, May. 2012.
- [36] Z. Lv, X. Gong, L. Liu, Z. Song and S. Zhou, "Parameters analysis and operation area calculation of VSG applied to distribution network," *CSEE JPES.*, doi: 10.17775/CSEEJPES.2019.02330
- [37] Microgrid Research Programme. (2014). [online] Available: www.microgrids.ct.aau.dk.